Journal of Solid State Chemistry 183 (2010) 2483–2489

Contents lists available at ScienceDirect

Journal of Solid State Chemistry

journal homepage: www.elsevier.com/locate/jssc

Structural characterization of the $FeTiO_3$–$MnTiO_3$ solid solution

Xiang Wu [a,*], Shan Qin [a], Leonid Dubrovinsky [b]

[a] Key Laboratory of Orogenic Belts and Crustal Evolution, MOE, Peking University and School of Earth and Space Sciences, Peking University, Beijing 100871, China
[b] Bayerisches Geoinstitut, Bayreuth University, Bayreuth D-95440, Germany

ARTICLE INFO

Article history:
Received 13 May 2010
Received in revised form
10 August 2010
Accepted 12 August 2010
Available online 18 August 2010

Keywords:
Ilmenite
Solid solution
X-ray diffraction
Mössbauer spectroscopy
Raman spectroscopy

ABSTRACT

We have synthesized the $(Mn_{1-x}Fe_x)TiO_3$ $(0.0 \le x \le 1.0)$ solid solution compounds by high-temperature sintered methods, and characterized their crystal structures by combining X-ray diffraction, Mössbauer spectroscopy and Raman spectroscopy. Lattice constants and volumes show a linear decrease with increase in $FeTiO_3$ content. All experimental results illustrate a decreasing distortion of TiO_6 (or FeO_6/MnO_6) octahedra with increase in $FeTiO_3$ content. The vibrational frequency of O–Ti–O bending motions presents a direct dependence on the corresponding bond angle (the ∠O–Ti–O).

1. Introduction

Ilmenite-type oxides with general formula ABO_3 are of widespread interest, not only in material science and crystal chemistry because of their diverse physical and chemistry properties, but also in geoscience because they are often found in many natural minerals from the Earth's depths, from the Moon surface and from meteorolite [1–7]. (Mg,Fe)SiO_3 ilmenite, for example, as the post enstatite phase, was discovered in the shock vein of meteorite that was named akimotoite [3]. It is stable at conditions of 21–23 GPa and 1473–1873 K, and is believed to be one of the essential phases in the lower part of the transition zone.

In nature there are several common ilmenite-group titanates as accessory minerals in kimberlites, igneous and metamorphic rocks, such as ilmenite, geikielite, pyrophanite and ecandrewsite. These titanates can crystallize series of complete solid solution systems, such as $Mg_{1-x}Fe_xTiO_3(0.0 \le x \le 1.0)$, $Mn_{1-x}Zn_xTiO_3$ $(0.0 \le x \le 1.0)$, $(Mn_{1-x}Fe_x)TiO_3(0.0 \le x \le 1.0)$ [8–11]. Accurate determination of their crystal structures is not an easy task because of most samples in micrometer scale have some impurities. In general, corresponding synthetic products are applied to analyze and discuss their crystal structure and chemistry. As far as we know, the crystal chemistry of the $(Mn_{1-x}Fe_x)TiO_3$ system has not been reported.

$FeTiO_3$, the end member of the $(Mn_{1-x}Fe_x)TiO_3$ system, undergoes phase transitions from the ilmenite to the perovskite on compression up to 20 GPa, and from the perovskite to the lithium niobate on decompression [12–14]. Thus it becomes a sensitive indicator of mineralogical or petrological processes, such as a geo-barometer for $FeTiO_3$-bearing rocks that may occur in shocked samples or being exhumed from the deep mantle. For example, recently a natural mineral $LiNbO_3$-type $FeTiO_3$ consisting of polysynthetic twin components observed by optical microscopy has been discovered in shocked gneiss from the Ries crater, which indicates that the Ries crater suffered at least 20 GPa shock pressure [15]. The other end member, $MnTiO_3$, has similar high-pressure behavior, with a lower phase-transition pressure of 3 GPa [16]. Knowledge of the crystal chemistry properties for the $(Mn_{1-x}Fe_x)TiO_3$ system is of significant interest at high pressure in Earth sciences. However, lack data of the $(Mn_{1-x}Fe_x)TiO_3$ system at ambient condition is seriously inadequate to analyze further the high-pressure properties.

Based on the above elaboration, the aim of this present work therefore is to synthesize the $(Mn_{1-x}Fe_x)TiO_3$ solid solution and characterize their crystal chemistry by combining X-ray diffraction (XRD), Mössbauer spectroscopy (MS) and Raman spectroscopy.

2. Experimental

Several polycrystalline samples in the $(Mn_{1-x}Fe_x)TiO_3$ $(0 \le x \le 1)$ solid solution were synthesized by standard solid-state reaction. Stoichiometric amounts of $MnCO_3$ (99.9%), Fe_2O_3 (99.998%) and TiO_2 (99.998%) were mixed and ground under ethanol in an agate mortar. The mixtures were compressed into

* Corresponding author.
E-mail address: xiang.wu@pku.edu.cn (X. Wu).

0022-4596/$ - see front matter Crown Copyright © 2010 Published by Elsevier Inc. All rights reserved.
doi:10.1016/j.jssc.2010.08.020

Table 1
Crystal data of the $(Mn_{1-x}Fe_x)TiO_3$ ($0.0 \le x \le 1.0$) system. The numbers in parentheses are the estimated standard deviations in units of the last digit.

$xFeTiO_3$	Ideal Real	0.0 0.0008	0.2 0.192	0.4 0.395	0.5 0.492	0.6 0.592	0.8 0.791	1.0 0.9994
a/Å		5.13935(7)	5.13009(6)	5.11913(7)	5.11445(7)	5.10962(9)	5.09912(6)	5.08894(7)
c/Å		14.2833(3)	14.2415(2)	14.2023(3)	14.1834(3)	14.1648(3)	14.1287(2)	14.0928(3)
V/Å^3		326.720(11)	324.591(9)	322.318(9)	321.300(9)	320.271(14)	318.144(8)	316.071(9)
Fe/Mn	z	0.3609(5)	0.3607(3)	0.3599(4)	0.3596(4)	0.3592(4)	0.3593(3)	0.3584(3)
(00z)	B(Å^2)	0.021(4)	0.036(3)	0.051(3)	0.052(4)	0.050(3)	0.056(2)	0.062(2)
Ti	z	0.1444(5)	0.1455(3)	0.1464(4)	0.1465(4)	0.1464(4)	0.1466(3)	0.1467(3)
(00z)	B(Å^2)	0.003(4)	0.013(2)	0.008(2)	0.022(3)	0.008(2)	0.004(2)	0.008(2)
O	x	0.3188(21)	0.3185(16)	0.3192(23)	0.3195(20)	0.3196(19)	0.3201(17)	0.3199(12)
(xyz)	y	0.0294(30)	0.0286(30)	0.0282(42)	0.0278(36)	0.0276(34)	0.0277(29)	0.0276(23)
	z	0.2417(11)	0.2411(7)	0.2405(8)	0.2401(7)	0.2396(6)	0.2395(5)	0.2393(4)
	B(Å^2)	0.015(3)	0.031(2)	0.037(3)	0.033(2)	0.013(2)	0.023(2)	0.022(2)
wRp (%)		4.5	4.3	4.6	4.6	5.4	5.8	8.0
Rp (%)		2.6	2.7	2.7	2.9	3.6	4.0	5.6
GOF		1.2	1.3	1.2	1.2	1.2	1.7	2.4

pellets with a diameter of 3 mm. These pellets were then heated in an open Pt capsule at 1200 °C for 24 h in CO–CO_2 gas mixtures corresponding to oxygen fugacity ($fO_2 = 10^{-11}$). Samples were drop quenched and examined *ex situ* by the JEOL JXA-8200 electron microprobe with an accelerating voltage of 15 kV and a beam current of 15 nA. Compositions are listed in Table 1 as mole fraction of $xFeTiO_3$.

Structures of the $(Mn_{1-x}Fe_x)TiO_3$ ($0 \le x \le 1$) solid solution were determined by means of room-temperature XRD in a Philips X'Pert diffractometer with Co $K\alpha_1$ radiation. An accelerating voltage of 40 kV and a beam current of 40 mA were applied. Powdered silicon (NBS) was mixed with the sample as an internal standard. Data were recorded between 20° and 120° of 2θ with steps of 0.033°, and a total collecting time of every diffraction pattern was 13 h. Data were analysed using the Rietveld method as implemented by the GSAS software [17]. Refined parameters include zero shifting, histogram scale factors, background coefficients, lattice parameters, profile parameters, atomic positions, thermal parameters and phase fractions.

Mössbauer spectra were measured in transmission mode on a constant acceleration Mössbauer spectrometer using a high specific activity ^{57}Co point source in a Rh matrix. The velocity scale was calibrated relative to a 25 μm-thick α-Fe foil. Samples weights for Mössbauer spectroscopy were calculated to provide the optimum sample thickness to reduce thickness effects. The sample diameter was 1.2 cm, and circa 4.94 mg Fe/cm^2 was used for all samples. The distance between sample and source was 7 cm, and that between sample and detector was 13 cm. Collection time for each spectrum was 12 h. Mössbauer spectra were fitted to Lorentzian line-shapes using the commercial software NORMOS written by R A Brand (distributed by Wissenschaftliche Elektronik GmbH, Germany).

Raman spectra of samples were recorded using the LabRam spectrometer in a back-scattering geometry. The 632.8 nm 100 mW He–Ne laser was used for excitation. The incident laser beam was focused on the sample using a 50× objective. Collecting time for each spectrum was 10 min.

3. Results and discussions

3.1. X-ray diffraction

Except diffraction peaks from Si (internal standard), the rest of the pattern could be indexed within ilmenite-type structure, which confirms a single phase for synthetic product without any impurity. No peaks merged and no new peaks appeared at various compositions, which indicate a complete solid solubility across the entire compositional range. Fig. 1 shows one example ($Fe_{0.5}Mn_{0.5}TiO_3$) analysed by the Rietveld refinement. All lattice constants, atom coordinates and their isotropic temperature factors are extracted and listed in Table 1. The results of both end members ($FeTiO_3$ and $MnTiO_3$) are well consistent with previous results [13,16]. The a, c axial length and unit-cell volume represent a linear-manner decrease with increase in $xFeTiO_3$ content (Fig. 2), because small size Fe^{2+} cations substitute for larger size Mn^{2+} cations in octahedral coordination. The c/a ratio also decreases linearly with increase in $xFeTiO_3$ content (Fig. 2), which implies the contribution of Fe^{2+} is anisotropy on the c-axis length and the a-axis length. It is in agreement with previous study that the electron density distributions around cations are not spherical, but elongated along the direction of the c-axis in ilmenite structure [18].

The ABO_3-type ilmenite structure is based on a hexagonal-close-packed oxygen lattice with metal atoms (A and B) occupying two-thirds of the available octahedral sites. Each octahedron shares three edges with octahedra inside the layer, a face with an octahedron of the second type of cation in the adjacent layer and the opposite face with a vacant octahedral site. Along the c-axis, layers of Fe and Ti alternate with a cation ordering of –Ti–Fe–V–Fe–Ti– (V: vacant sites). A and B coordinates deviate from the ideal center of their octahedra (0,0,1/3) and (0,0,1/6), respectively. With increase in $xFeTiO_3$ content, the Fe/Mn and Ti coordinates shift toward the center of octahedra along the c-axis (Table 1), meaning that the distortions of octahedra decrease. Bond lengths of Fe/Mn–O, Ti–O and Fe/Mn–Ti are plotted as a function of $xFeTiO_3$ content in Fig. 3. Three A–O (or B–O) bond lengths (shared face) are longer than those of the A–O (or B–O) (unshared face). The difference between them shows a decrease in bond length with increase in $xFeTiO_3$ content. This behavior of the Fe/Mn–O and Ti–O bond lengths imply Fe^{2+} instead of Mn^{2+} can reduce the distortions of octahedra. The repulsive force between Fe/Mn and Ti along the c-axis is enhanced because their distances become shorter with increase in $xFeTiO_3$ content (Fig. 3). In order to quantitatively describe octahedral distortion, a conventional expression was adopted: the quadratic elongation $\langle \lambda \rangle = \sum_i^6 (l_i/l_0)^2/6$, where l_0 is the center-to-vertex distance for an ideal octahedron with O_h symmetry, whose value is equal to that of a distorted octahedron with bond length l_i [19]. Fig. 4 shows the relations between the quadratic elongation and the composition. In the $FeTiO_3$–$MnTiO_3$ system, the distortions of TiO_6 octahedra are less than those of FeO_6(MnO_6) octahedral.

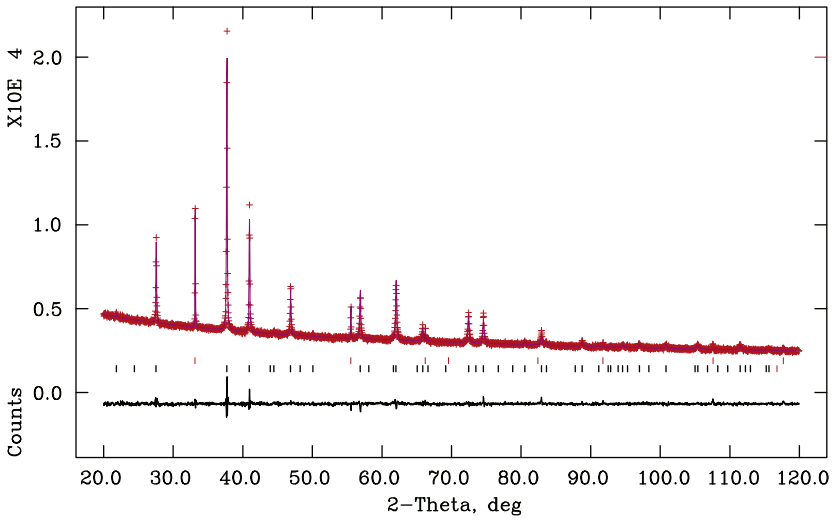

Fig. 1. XRD pattern analysis of an example $(Mn_{0.5}Fe_{0.5})TiO_3$ by the Rietveld method. Data are indicated by +, and calculated pattern by the pink solid line. The different pattern is shown at the bottom. The locations of reflections are indicated by the vertical bars: upper row for internal standard silicon and lower row for $(Mn_{0.5}Fe_{0.5})TiO_3$. (For interpretation of the references to color in this figure legend, the reader is referred to the web version of this article.)

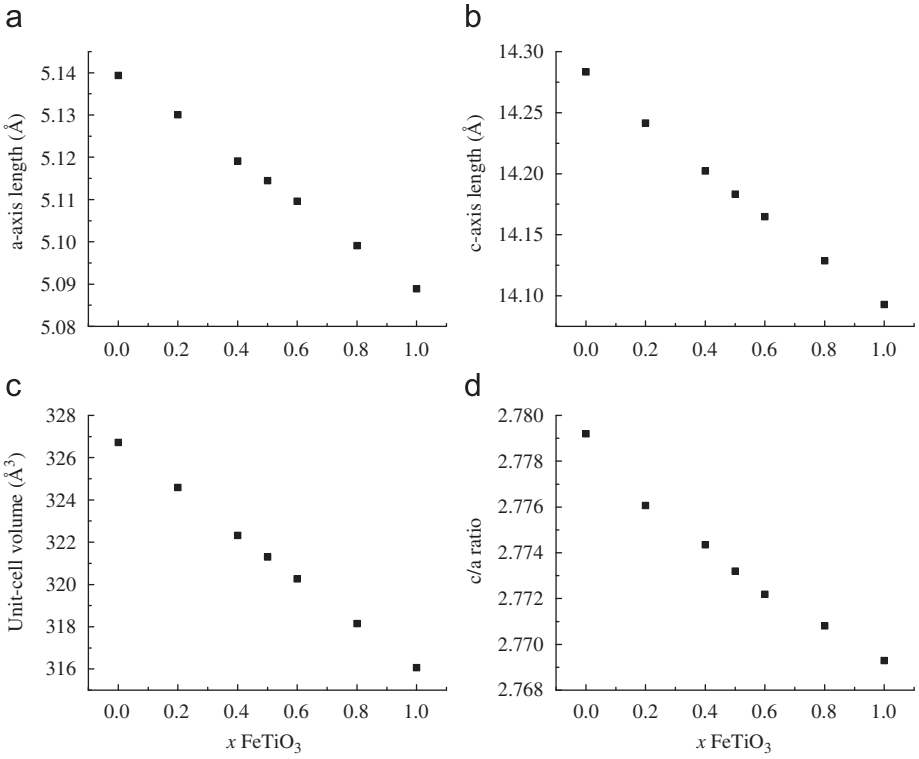

Fig. 2. Lattice constant as a function of xFeTiO$_3$ content. (a) the a-axis, (b) the c-axis, (c) volume and (d) the c/a ratio.

The behavior of the quadratic elongation also supports the observation that the octahedral distortions decrease with increase in xFeTiO$_3$ content.

The bond valence sum (*BVS*) for cations were calculated from six M–O bond lengths in MO_6 octahedra according to the formula $BVS = \sum_{i=1}^{n} \exp((R_i - R_0)/0.37)$, where R_i is the bond length and R_0 is the bond valence parameter [20]. Here R_0 of A site cation is equal to $(1-x)R_0(\mathrm{Mn}) + xR_0(\mathrm{Fe})$ in the $Mn_{1-x}Fe_xTiO_3$ system [21]. Fig. 4(b) plots the *BVS* values as a function of xFeTiO3 content. It is very obvious that oxidation state of A site cations (Mn/Fe) decreases and that of B site cation (Ti) increase with increase in Fe-doping content.

3.2. Mössbauer spectroscopy

Several typical spectra are shown in Fig. 5. The spectrum shows a well-resolved doublet attributed to a Fe^{2+} component in an octahedral environment and a Fe^{3+} singlet. Fe hyperfine parameters (isomer shift δ, and quadrupole splitting ΔE_Q) are

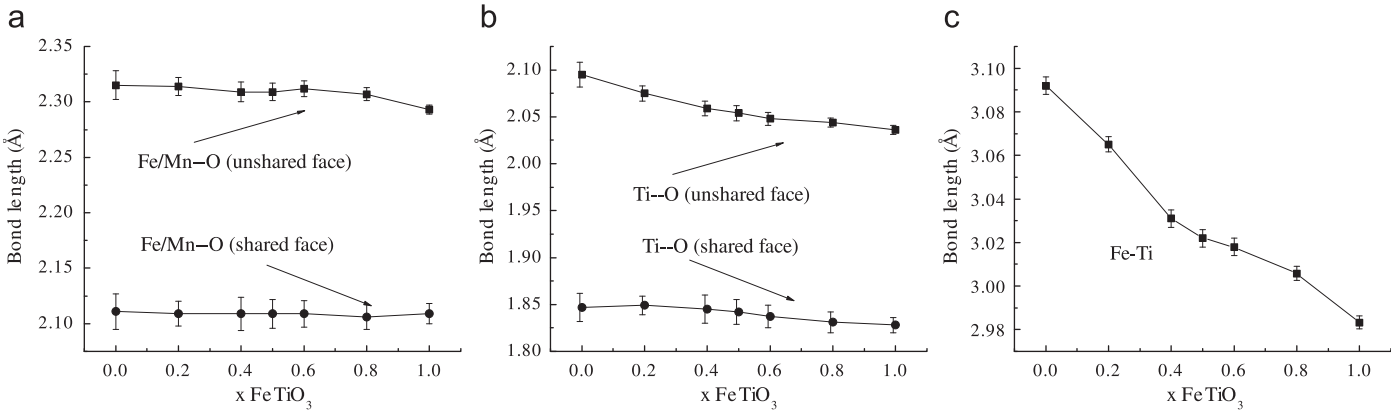

Fig. 3. Bond length as a function of xFeTiO$_3$ content. (a) the Fe/Mn–O distance, (b) the Ti–O distance and (c) the Fe–Ti distance along the c-axis.

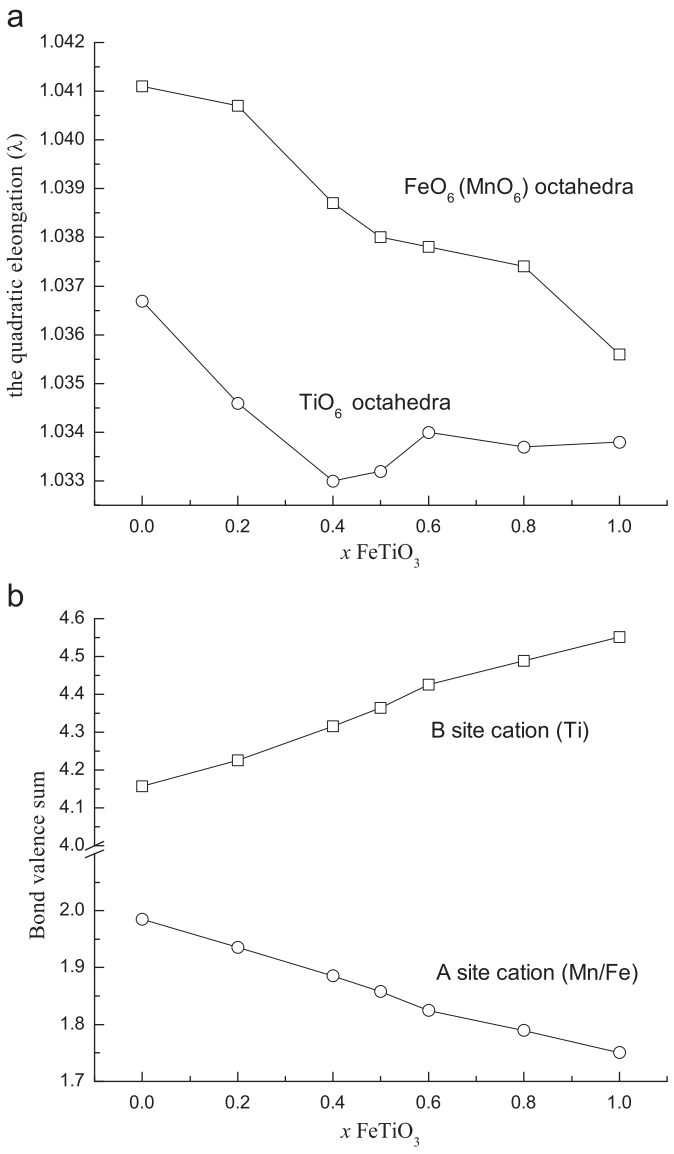

Fig. 4. (a) The relationship between the quadratic elongation and xFeTiO$_3$ content and (b) the bond valence sum for A and B site cations as a function of xFeTiO$_3$ content.

listed in Table 2 and plotted in Fig. 6 as a function of xFeTiO$_3$ composition. In all samples Fe^{3+} contents are similar only 3–6%. For end-member FeTiO$_3$, We observed $\delta=1.058(1)$ mm/s and $\Delta E_Q=0.684(1)$ mm/s for Fe^{2+} component, consistent with values reported in the previous literatures [13].

Hyperfine parameters are sensitive to the local environment of iron. The isomer shift depends on the valence and spin state of iron, and also on the sample density. Valence and spin state are the same in the $(Mn_{1-x}Fe_x)TiO_3$ $(0\le x\le 1)$ system, but the density increases with increase in Fe content (Fig. 2c), which results in a smaller isomer shift. The quadrupole splitting for high-spin Fe^{2+} in octahedral coordination could be $\Delta E_Q=\Delta E_Q(0)\alpha^2F(\Delta_1, \Delta_2, \lambda_0, \alpha^2, T)$, where $\Delta E_Q(0)$ is the maximum possible value of the quadrupole splitting, F is the reduction function whose value is given by perturbation theory, Δ_1 and Δ_2 are the two lowest splitting of the crystal-field levels, α^2 is a covalence factor, λ_0 is a spin-orbit coupling constant, and T is the absolute temperature [22]. The roles of α^2 and λ_0 on the quadrupole splitting are neglected for simplicity. Thus, ΔE_Q is described to be $\Delta E_Q(0)F(\Delta_1, \Delta_2, T)$. In general, the values of Δ_1 and Δ_2 can be used to express the octahedral distortion. Ingalls [22] demonstrated that the quadrupole splitting increases very rapidly with increasing octahedral distortion at small distortions, then reaching a maximum. Thus the behavior of Fe^{2+} ΔE_Q as a function of xFeTiO$_3$ (Fig. 6) indicates that FeO$_6$ (MnO$_6$) distortion decreases with increase in xFeTiO$_3$ content, in well consistent with XRD results.

Fig. 7 shows the relations between the quadratic elongation and the quadrupole splitting. The quadrupole splitting increases from 0.683 to 0.801 mm/s at small distortions (λ from 1.0354 to 1.0385), then reaches a maximum value (0.801 mm/s). The phenomenon observed in our study is in agreement with the model proposed by Ingalls [22].

3.3. Raman spectroscopy

For ilmenite-type structure (ABO$_3$-type), group theoretical calculation yields ten Raman active phonon modes $\Gamma=5A_g+5E_g$ in the first-order Raman spectrum [23]. Each Raman model was assigned based on ionic substitution: $A_{g(1)}$ and $E_{g(1)}$ to B^{4+}–O stretching motions; $A_{g(2)}$, $A_{g(3)}$, $E_{g(2)}$ and $E_{g(3)}$ to O–B^{4+}–O bending motions; $A_{g(4)}$ and $E_{g(4)}$ to translations of the BO$_6$ octahedra against A^{2+} cations; $A_{g(5)}$ and $E_{g(5)}$ to translations of the A^{2+} cation against the oxygen framework [2]. In the present experiments on polycrystalline samples, nine clear Raman models were observed except one model $E_{g(2)}$. For the end-member MnTiO$_3$, nine positions of Raman peaks (166, 203, 237, 264, 335, 359, 467, 601 and 685 cm^{-1}) are in good agreement with previous values (168, 202, 235, 264, 335, 360, 468, 599 and 682 cm^{-1}) [24].

In the present study, increase in xFeTiO$_3$ content in the $(Mn_{1-x}Fe_x)TiO_3$ $(0\le x\le 1)$ system results in two kinds of Raman shifting behaviors: $E_{g(3)}$ shifts to high frequency and the

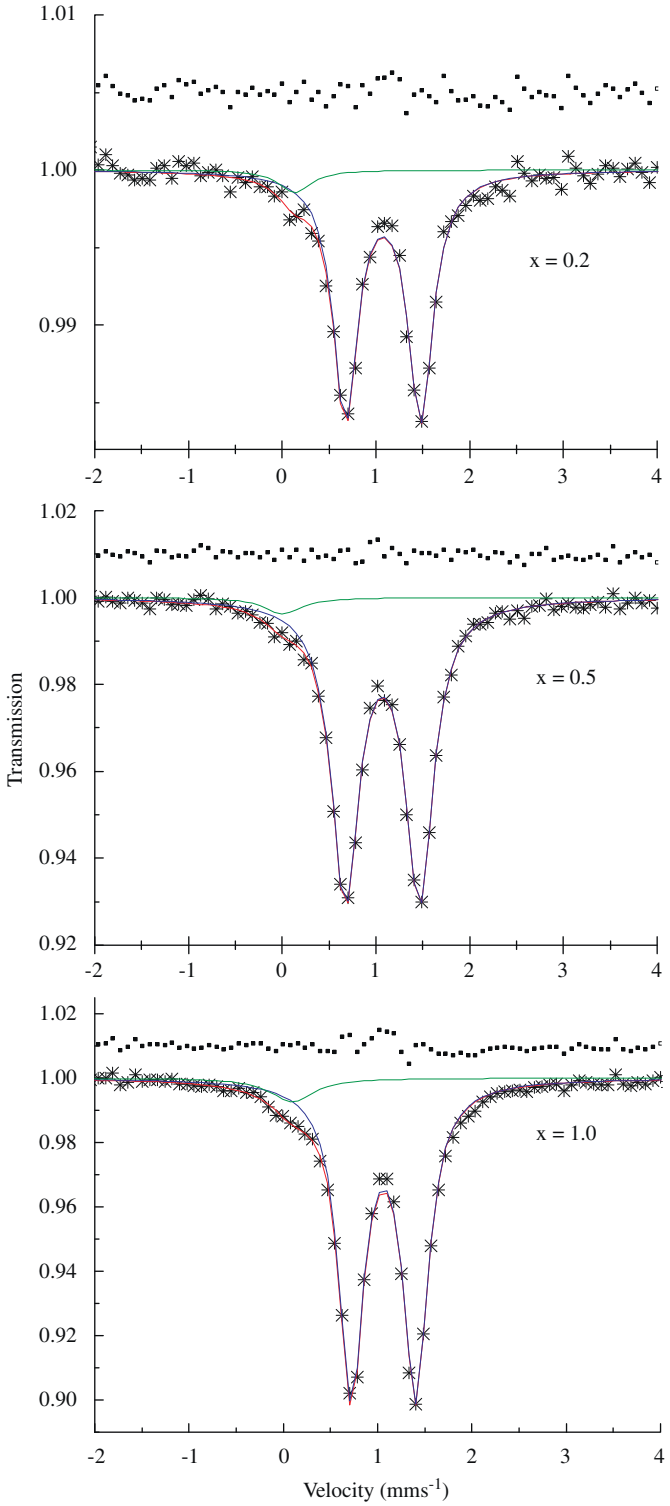

Fig. 5. Several selected Mössbauer spectra of the $(Mn_{1-x}Fe_x)TiO_3$ $(0.0 \le x \le 1.0)$ system. The doublet is assigned to Fe^{2+} in octahedral environment, and the singlet corresponds to Fe^{3+} component.

Table 2
Iron hyperfine parameters in the $(Mn_{1-x}Fe_x)TiO_3$ $(0.0 \le x \le 1.0)$ system. Γ is the full width at half maximum, and A is the ratio of area. The numbers in parentheses are the estimated standard deviations in units of the last digit.

xFeTiO$_3$	Octahedral Fe^{2+}				Fe^{3+}		
	δ (mm/s)	ΔE_Q (mm/s)	Γ (mm/s)	A (%)	δ (mm/s)	Γ (mm/s)	A (%)
0.2	1.076(3)	0.802(6)	0.316(9)	94(2)	0.18(6)	0.41(19)	6(2)
0.4	1.070(2)	0.793(3)	0.340(4)	94(1)	−0.08(5)	0.72(18)	6(1)
0.5	1.068(1)	0.792(3)	0.354(4)	96(1)	−0.11(5)	0.47(15)	4(1)
0.6	1.061(3)	0.783(5)	0.359(8)	100			
0.8	1.059(1)	0.732(2)	0.346(3)	97(1)	−0.15(3)	0.42(11)	3(1)
1.0	1.058(1)	0.684(1)	0.319(2)	94(1)	−0.21(1)	0.56(6)	6(1)

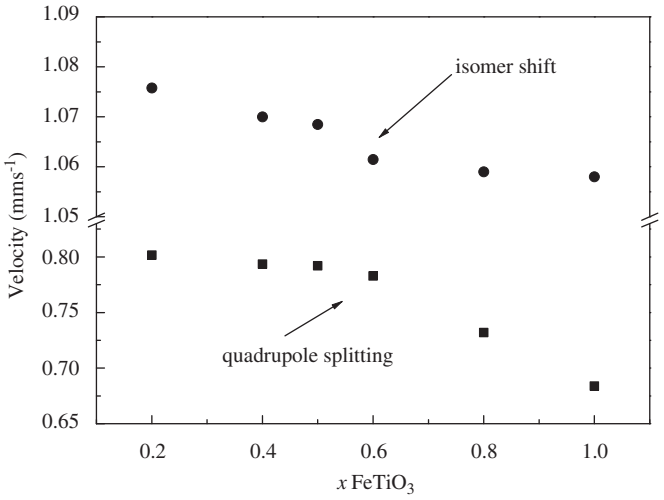

Fig. 6. Iron hyperfine parameters (δ and ΔE_Q) as a function of xFeTiO$_3$.

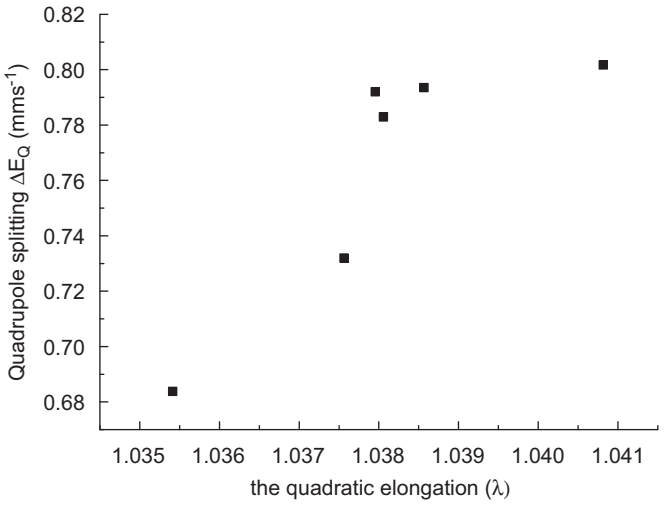

Fig. 7. Fe^{2+} quadrupole splitting as a function of the quadratic elongation for FeO_6 octahedra.

remaining shifts to low frequency (Figs. 8 and 9). Hofmeister [2] summarized the behavior of vibrational frequencies of eight ilmenite-type compounds, and proposed that the six highest frequencies increase as the cell volume decreases, and the four lowest frequency modes depended on mass of the divalent cations. Here the four lowest frequencies shift to lower values, attributed to the heavy Fe atom substitution of Mn atom in A sites. However, the behavior of six high frequencies is complex, which is contradictory to Hofmeister's semi-empirical results [2]. The simple harmonic oscillator model cannot explain the behavior of the six high frequencies although their corresponding bond lengths decrease with increase in xFeTiO$_3$ content (Fig. 3). The most likely reasons include the neglecting of the near-neighbor interactions and crystal field effects [25]. In addition to the

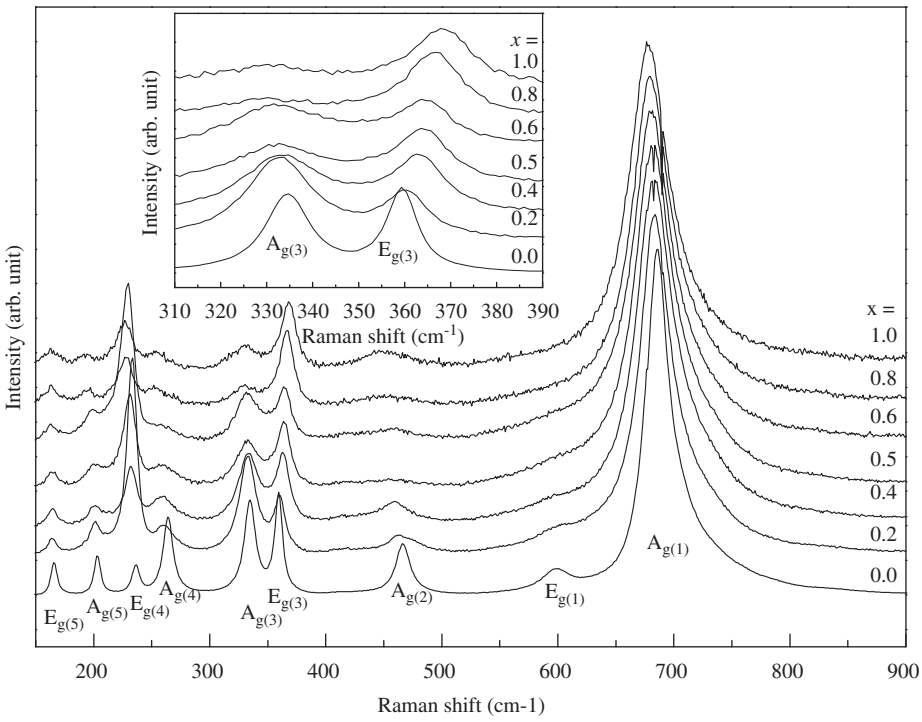

Fig. 8. Raman spectra of the $(Mn_{1-x}Fe_x)TiO_3$ $(0.0 \le x \le 1.0)$ system. Inset: the enlarged view from 310 to 390 cm^{-1}.

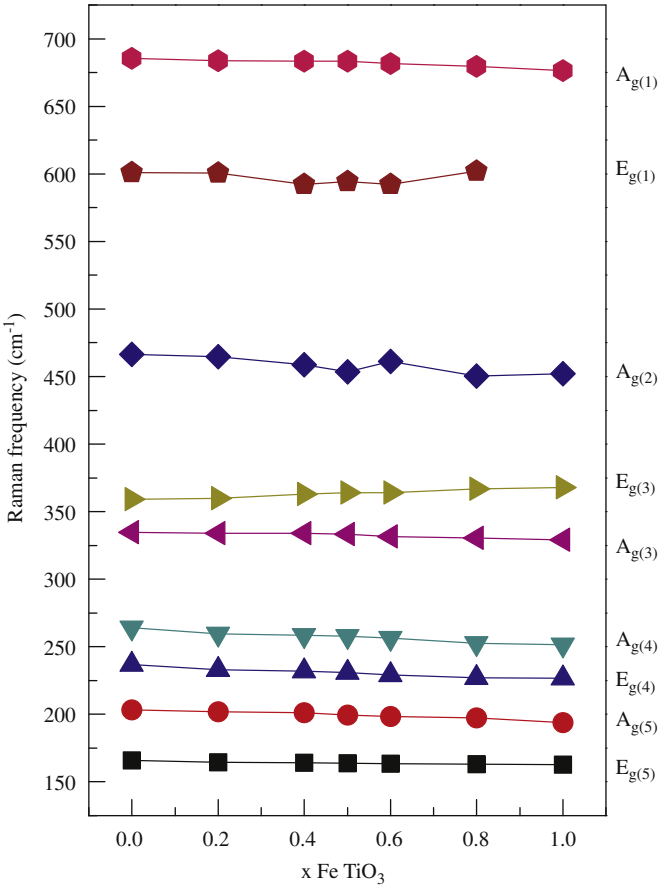

Fig. 9. Raman shift of nine bands as a function of xFeTiO$_3$ content.

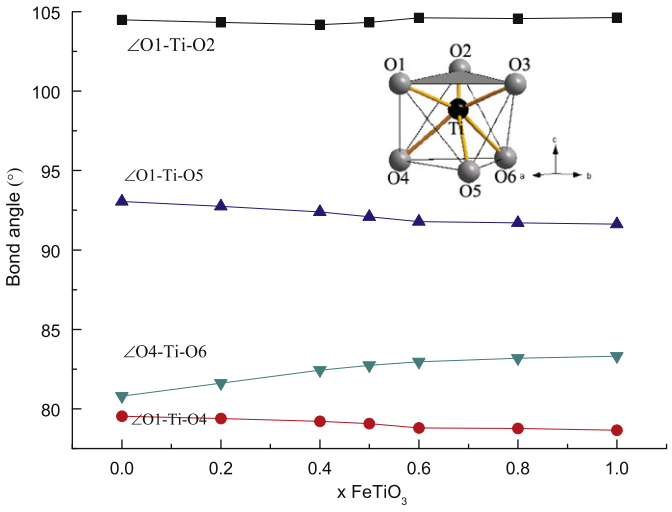

Fig. 10. Four O–Ti–O bending motions as a function of xFeTiO$_3$ content. Inset: TiO_6 an octahedron sketch, black ball is the Ti atom and the gray is the oxygen atom, gray triangle is a shared plane with FeO_6/MnO_6 octahedron.

cation–anion force constant, the anion–anion force constant in the octahedron should be considered. Two highest models ($A_{g(1)}$ and $E_{g(1)}$) are Ti–O stretching motions, which can qualitatively reflect the distortion of TiO_6 if the net effects of the Ti–O force constant and the O–O force constant are taken into account [26]. The decrease of $A_{g(1)}$ and $E_{g(1)}$ frequencies indicates a less distortion of the TiO_6 octahdera, which is consistent with our above XRD and MS results, also similar to the behavior of the SiO_4 tetrahedra in the forsterite–monticellite solid solutions [26]. The bond angle (∠O–Ti–O) is obviously directly relative to the net effects of the Ti–O and the O–O interaction. Four bond angles (∠O1–Ti–O4, ∠O1–Ti–O2, ∠O1–Ti–O5 and ∠O4–Ti–O6), therefore, were adopted to qualitatively describe the O–Ti–O bending motions $A_{g(2)}$, $A_{g(3)}$, $E_{g(2)}$ and $E_{g(3)}$, respectively (Fig. 10). Except $E_{g(2)}$ band unobserved, $A_{g(2)}$, $A_{g(3)}$ and $E_{g(3)}$ frequencies show a direct dependence on the corresponding bond angles: the ∠O4–Ti–O6 increasing, the corresponding frequencies $E_{g(3)}$ increasing; for the rest of the angles decreasing, the rest the frequencies are decreasing.

In addition, the linewidths of Raman bands broaden with increase in xFeTiO$_3$ content. Especially, the intensity of $E_{g(1)}$ becomes very weak so that it is very hard to identify. The results demonstrate that the linewidths are sensitive to small changes in ionic size, even the ions are with the same charge and the same coordination number.

4. Conclusion

Seven samples of the $(Mn_{1-x}Fe_x)TiO_3$ $(0.0 \le x \le 1.0)$ system were prepared and structurally characterized by combining X-ray diffraction, Mössbauer spectroscopy and Raman spectroscopy. XRD results illustrate that the $(Mn_{1-x}Fe_x)TiO_3$ system is a complete solid solubility across the entire compositional range with ilmenite-type structure. Lattice constants and volumes show a linear decrease with increase in $FeTiO_3$ content. A less distortion of TiO_6 (or FeO_6/MnO_6) octahedra represents with increase in $FeTiO_3$ content, supported by XRD, MS and Raman spectroscopy results. The dominant oxidation state is ferrous in the $(Mn_{1-x}Fe_x)TiO_3$ $(0.0 \le x \le 1.0)$ system. There are two kinds of Raman frequencies shifting behaviors: $E_{g(3)}$ shifts to high frequency and the remaining shifts to low frequency with increase in xFeTiO$_3$ content. The vibrational frequency of O–Ti–O bending motions presents a direct dependence on the corresponding bond angle (the $\angle$O–Ti–O).

Acknowledgments

The authors would like to thank T. Boffa-Ballaran and C. McCammon for their assistances in XRD and MS experiments. X. Wu is grateful for his Alexander von Humboldt Fellowship and the financial support of the National Natural Science Foundation of China (Grant no. 40972029).

References

[1] K.N. Raymond, H.R. Wenk, Contrib. Mineral. Petrol. 30 (1971) 135.
[2] A.M. Hofmeister, Eur. J. Mineral. 5 (1993) 281.
[3] N. Tomioka, K. Fujino, Science 277 (1997) 352.
[4] A. Agui, M. Mizumaki, Y. Saitoh, T. Matsushita, T. Nakatani, A. Fukaya, E. Torikai, J. Synchrotron Rad 8 (2001) 907.
[5] T. Yamanaka, Y. Komatsu, M. Sugahara, T. Nagai, Am. Miner. 90 (2005) 1301.
[6] G. Radtke, S. Lazar, G.A. Botton, Phys. Rev. B 74 (2006) 155117.
[7] A. Okada, T. Narita, T. Nagai, T. Yamanaka, Am. Miner. 93 (2008) 39.
[8] R.H. Mitchell, R.P. Liferovich, Can. Miner. 42 (2004) 1169.
[9] R.H. Mitchell, R.P. Liferovich, Can. Miner. 42 (2004) 1871.
[10] R.H. Mitchell, R.P. Liferovich, Phys. Chem. Miner. 32 (2005) 442.
[11] R.H. Mitchell, R.P. Liferovich, Can. Miner. 44 (2006) 1099.
[12] L.C. Ming, Y.H. Kim, T. Uchida, Y. Wang, M. Rivers, Am. Miner. 91 (2006) 120.
[13] X. Wu, G. Steinle-Neumann, O. Narygina, I. Kantor, C. McCammon, S. Pascarelli, G. Aquilanti, V. Prakapenka, L. Dubrovinsky, Phys. Rev. B 79 (2009) 094106.
[14] X. Wu, G. Steinle-Neumann, O. Narygina, C. McCammon, and L. Dubrovinsky, High Press. Res., accepted for publication, doi:10.1080/08957959.2010.484284.
[15] L. Dubrovinsky, A. El Goresy, P. Gillet, X. Wu, A. Simionivici, Meteorit. Planet. Sci. 44 (2009) A64.
[16] N.L. Ross, C.T. Prewitt, Phys. Chem. Miner. 16 (1989) 621.
[17] B.H. Toby, J. Appl. Crystallogr. 34 (2001) 210.
[18] T. Yamanaka, Y. Komatsu, Phys. Chem. Miner. 34 (2007) 307.
[19] K. Robinson, G.V. Gibbs, P.H. Ribbe, Science 172 (1971) 567.
[20] I.D. Brown, R.D. Shannon, Acta Crystallogr. A 29 (1973) 266.
[21] I.D. Brown, D. Altermatt, Acta Crystallogr. B 41 (1985) 244.
[22] R. Ingalls, Phys. Rev. 133 (1964) A787.
[23] W.G. Fateley, N.T. McDevitt, F.F. Bently, App. Spectrosc. 25 (1971) 155.
[24] J. Ko, C.T. Prewitt, Phys. Chem. Miner. 15 (1988) 355.
[25] P.K. Lam, R. Yu, M.W. Lee, S.K. Sharma, Am. Miner. 75 (1990) 109.
[26] K. Mohanan, S.K. Sharma, Am. Miner. 78 (1993) 42.